

System, centrality, and transverse mass dependence of two-pion correlation radii in heavy ion collisions at 11.6 and 14.6 A·GeV/c

L. Ahle,^{11,*} Y. Akiba,⁶ K. Ashktorab,² M. D. Baker,^{11,†} D. Beavis,² P. Beery,⁵ H. C. Britt,⁹ B. Budick,¹² J. Chang,⁵ C. Chasman,² Z. Chen,² C. Y. Chi,⁴ Y. Y. Chu,² V. Cianciolo,^{11,‡} B. A. Cole,⁴ J. B. Costales,¹¹ H. J. Crawford,³ J. B. Cumming,² R. Debbe,² J. C. Dunlop,^{11,§} W. Eldredge,⁵ J. Engelage,³ S. Y. Fung,⁵ E. Garcia,^{10,¶} M. Gonin,² S. Gushue,² H. Hamagaki,¹⁵ L. F. Hansen,⁹ R. S. Hayano,¹³ S. Hayashi,² G. Heintzelman,¹¹ S. Homma,⁶ E. Judd,¹¹ H. Kaneko,⁸ J. Kang,^{5,**} S. Kaufman,¹ W. L. Kehoe,¹¹ E. J. Kim,² A. Kumagai,¹⁴ K. Kurita,^{4,††} R. J. Ledoux,¹¹ J. H. Lee,² M. J. LeVine,² J. Luke,⁹ Y. Miake,¹⁴ A. Mignerey,¹⁰ D. P. Morrison,^{11,†} R. J. Morse,¹¹ B. Moskowitcz,² M. Moulson,⁴ C. Müntz,^{2,‡‡} S. Nagamiya,^{4,§§} M. N. Nambodiri,⁹ T. K. Nayak,⁴ C. A. Ogilvie,^{11,¶¶} J. Olness,² C. G. Parsons,¹¹ L. P. Remsberg,² D. Roehrich,^{2,***} P. Rothschild,¹¹ H. Sako,¹⁵ H. Sakurai,¹³ T. C. Sangster,⁹ R. Seto,⁵ J. Shea,¹⁰ K. Shigaki,⁶ R. A. Soltz,^{11,*} P. Stankus,^{4,‡} S. G. Steadman,^{11,†††} G. S. F. Stephans,¹¹ T. W. Sung,¹¹ Y. Tanaka,⁷ M. J. Tannenbaum,² J. H. Thomas,^{9,‡‡‡} S. R. Tonse,^{9,‡‡‡} S. Ueno-Hayashi,¹⁴ J. H. van Dijk,² F. Videbæk,² O. Vossnack,^{4,§§§} V. Vutsadakis,¹¹ F. Wang,^{4,¶¶¶} Y. Wang,⁴ H. E. Wegner,² D. Woodruff,¹¹ Y. Wu,⁴ H. Xiang,⁵ G. H. Xu,⁵ K. Yagi,¹⁴ X. Yang,⁴ H. Yao,¹¹ D. Zachary,¹¹ W. A. Zajc,⁴ and F. Zhu²

(E-802 Collaboration)

¹Physics Division, Argonne National Laboratory, Argonne, Illinois 60439-4843

²Brookhaven National Laboratory, Upton, New York 11973

³Space Sciences Laboratory, University of California at Berkeley, Berkeley, California 94720

⁴Columbia University, New York, New York 10027 and Nevis Laboratories, Irvington, New York 10533

⁵University of California at Riverside, Riverside, California 92507

⁶High Energy Accelerator Research Organization (KEK), Tanashi-branch, Tokyo 188, Japan

⁷Kyushu University, Fukuoka 812, Japan

⁸Kyoto University, Sakyo-Ku, Kyoto 606, Japan

⁹Lawrence Livermore National Laboratory, Livermore, California 94550

¹⁰University of Maryland, College Park, Maryland 20742

¹¹Laboratory for Nuclear Science, Massachusetts Institute of Technology, Cambridge, Massachusetts 02139

¹²New York University, New York, New York 10003

¹³Department of Physics, University of Tokyo, Tokyo 113, Japan

¹⁴University of Tsukuba, Tsukuba, Ibaraki 305, Japan

¹⁵Center for Nuclear Study, School of Science, University of Tokyo, Tanashi, Tokyo 188, Japan

(Dated: November 8, 2018)

Two-pion correlation functions are analyzed at mid-rapidity for three systems (14.6 A·GeV/c Si+Al, Si+Au, and 11.6 A·GeV/c Au+Au), seven distinct centrality conditions, and different k_T bins in the range 0.1–0.5 GeV/c. Source reference frames are determined from fits to the Yano-Koonin source parameterization. Bertsch-Pratt radius parameters are shown to scale linearly with both number of projectile and total participants as obtained from a Glauber model calculation. A finite emission duration that increases linearly with system/centrality is also reported. The m_T dependence of the Bertsch-Pratt radii is measured for the central Si+Au and Au+Au systems. The system/centrality dependence is investigated separately for both high and low m_T regions.

I. INTRODUCTION

Bose-Einstein correlations of identical charged pions were first observed and used to extract a source size for pion emission in $p\bar{p}$ annihilations [1]. This technique has since been applied to heavy ion collisions ranging in energy from 1.8 A·GeV/c at the Bevalac [2, 3] to $\sqrt{s_{NN}} = 130$ GeV at RHIC [4, 5] (see also recent reviews [6, 7] and references therein). Symmetrization of the two-pion wave function results in an enhancement of the two-particle correlation in a region of low relative momentum, the extent of which is inversely proportional to the size or radius of the emitting source. The technique is most commonly referred to as HBT, after the simi-

*Present address:LLNL, Livermore, CA 94550

†Present address:BNL, Upton, NY 11973

‡Present address:ORNL, Oak Ridge, TN 37831

§Present address:Yale Univ., New Haven, CT 06520

¶Present address:Univ. of Illinois, Chicago, IL 60607

**Present address:Yonsei Univ., Seoul 120-749, Korea

††Present address:RIKEN, Saitama 351-01, Japan

‡‡Present address:GSI, D-64291 Darmstadt, Germany

§§Present address:KEK, 1-1 Oho, Tsukuba, Ibaraki 305 Japan

¶¶Present address:Iowa State Univ., Ames, IA 50010

***Present address:Univ. of Bergen, 5007 Bergen, Norway

†††Present address:U.S. Dept. of Energy, Germantown, MD 20874

‡‡‡Present address:LBNL, Berkeley, CA 94720

§§§Present address:CERN, CH-1211, Geneva 23, Switzerland

¶¶¶Present address:Purdue Univ., West Lafayette, IN 47907

lar technique pioneered by Hanbury-Brown and Twiss to measure stellar radii from intensity interferometry with radio waves [8]. The form of the two-pion correlation depends upon the emission function assumed for the pion source. For static source distributions with no final state interactions, such as the Fermi Statistical Model first used by Goldhaber *et al.* [1], the correlation function is related to the square of the 3-dimensional Fourier transform of the source distribution, $\rho(\mathbf{r})$, with respect to the pion relative momentum, $\mathbf{q} = \mathbf{p}_1 - \mathbf{p}_2$,

$$C(\mathbf{p}_1, \mathbf{p}_2) \equiv \frac{P(\mathbf{p}_1, \mathbf{p}_2)}{P(\mathbf{p}_1)P(\mathbf{p}_2)} = 1 + |\bar{\rho}(\mathbf{q})|^2. \quad (1.1)$$

For a multi-dimensional, Gaussian parameterization of the source, the enhancement in the relative momentum correlation is given by a multi-dimensional Gaussian with each Gaussian width inversely proportional to the canonically conjugate dimension, or radius. For dynamic, rapidly expanding sources the radii decrease with increasing transverse mass, m_T , of the pion pair [9, 10, 11, 12, 13], where $m_T = \sqrt{k_T^2 + m_\pi^2}$, and k_T is the mean transverse momentum of the pion pair. These m_T -dependent radii correspond to the relative separations of the pions with low relative momentum and are commonly referred to as “lengths of homogeneity”.

Interest in measuring source sizes in heavy ion collisions comes partly from the expectation that the presence of a QCD phase transition will lead to large source sizes and long lifetimes for particle emission [10, 14, 15]. The absence of such a signal, coupled with the complex and subtle nature of the m_T dependence, has left many puzzled over how best to interpret the available HBT results. However, in heavy ion collisions, there exists additional geometric information from the size of the system, the centrality of the collision, and also the reaction plane. Results on the pion source shape relative to the reaction plane for non-central collisions [16, 17] provide one important confirmation that HBT radii are strongly correlated with physical dimensions of the nuclear overlap region. A previous comparison of HBT sources to nuclear geometry [18] also confirmed this correlation, but the compilation included different source parameterizations, online triggers, and experimental acceptances.

We present a study of the dependence of the radii on system size and centrality for the two-pion correlation function from 14.6 A·GeV/c Si+Al, Si+Au, and 11.6 A·GeV/c Au+Au collisions at the BNL AGS measured by the E802 rotating magnetic spectrometer (Henry Higgins). The radii are compared to three geometric quantities: the effective nuclear radius for the number of projectile participants, the radius for the total participants, and the transverse distribution of binary collisions calculated with a Glauber model. The data sets of the three systems span a range of seven distinct nuclear geometries. The m_T dependence is examined for the high statistics central Si+Au and Au+Au systems and compared to measurements of Au+Au central collisions by the E866 Forward Spectrometer. Furthermore,

the centrality dependence is investigated separately for high and low values of m_T for all systems.

Sec. II describes the experimental apparatus relevant to this analysis. Sec. III covers the data reduction. The correlation analysis procedure is described in Sec. IV and results are presented in Sec. V. The conclusions are given in Sec. VI. Appendix C contains the complete set of tables for the correlation radii. A Monte Carlo study to check systematic effects in the Yano-Koonin fits is presented in Appendix A. Details and systematic studies of the Coulomb correction are provided in Appendix B.

II. EXPERIMENT

The Si+Al/Au data were collected in 1991 and 1992 by BNL E859, and the Au+Au data were collected in 1992 and 1994 by BNL E866. Both experiments were extensions of BNL E802. This series of experiments ran in the B1 line of the Brookhaven AGS from 1986 through 1995. The complete experimental setups are described elsewhere [19, 20]. The components essential for this analysis are a Target Multiplicity Array (TMA), a Zero-degree Calorimeter (ZCAL) [21], a series of four drift chambers (T1–T4), two trigger chambers (TR1, TR2), two multi-wire proportional chambers (TRF1, TRF2) a time of flight wall (TOF), beam counters (BC), and a level-2 trigger (LVL2).

The TMA measured total charged particle multiplicity from resistive tube pads configured in a wall and barrel array surrounding the target. A sum of the discriminated pad signals was used in the level-1 trigger to enhance both central and peripheral data sets. The TMA was present only for the Si beam and was removed prior to the Au beam commissioning in 1992. The ZCAL consisted of alternating layers of Pb and scintillator and was placed 11 m downstream from the target. It was completely rebuilt and incorporated into the level-1 trigger prior to the start of Au beam in 1992. For the data sets presented here the rms energy resolution ranged from $2.0\sqrt{E}$ for the Si beam to $3.2\sqrt{E}$ for the Au beam.

Beam definitions and t_0 for TOF were provided by upstream beam counters (BC) in anti-coincidence with a series of veto paddles. The interaction trigger condition was established by a bullseye (BE) scintillator detector, placed just before the ZCAL. For the Au beam, this was replaced by a Čerenkov radiator. The interaction trigger was defined by $Z < 26.5$ for the Si Beam, and $Z < 73$ for the Au beam.

The four drift chambers were placed two before and two after the magnet. T1, T2, T3, and T4, were positioned approximately 1, 1.5, 4, and 4.5 m downstream from the target, respectively. The drift chambers provided a position resolution of $150 \mu\text{m}$, and a minimum two-track separation of 2 mm. For this analysis, the magnet was run at 0.4 Tesla, for an integrated field of 0.585 T·m. The trigger chambers, TR1 and TR2, were located behind T3 and T4, respectively. For the 1994 running,

two highly segmented multi-wire chambers, TRF1 and TRF2 were added behind T1 and T2, respectively, to improve track reconstruction in the higher multiplicity environment. Resolutions for the TRF chambers were approximately $200 \mu\text{m}$. The TOF was placed about 6 m downstream and particle flight times were measured with an rms resolution of 120 ps.

The level-2 trigger (LVL2) was an integral part of the data taking and was especially important for collecting two-pion events in peripheral collisions. It consisted of TR1, TR2, TOF, and a series of LeCroy CAMAC modules used for fast readout, hit storage, memory lookup, and logic [22]. The trigger algorithm looped over all TR1-TOF hit combinations and matched hits on TR2 for tracks projected from the target. Momentum and $1/\beta$ for valid combinations were determined through lookup tables based on hit positions and time-of-flight. One or two independent regions in mass vs. momentum could be specified in any logical combination to form the trigger condition. All events for which the LVL2 did not produce a veto within $40 \mu\text{sec}$ were accepted. A set of events in which the LVL2 decision was recorded but not used to veto were collected for each LVL2 condition used in the experiment. All data sets presented here made use of the level-2 trigger, sometimes in combination with a level-1 centrality trigger in the TMA or ZCAL. LVL2 rejection factors ranged from 3–10 for Au+Au central to Si+Al peripheral events. Trigger inefficiencies were determined to be of order 1% for these data, and were dominated by the wire chamber inefficiencies. No detectable trigger bias was found for the two-pion data sets.

Nine data sets were taken covering seven different system and centrality conditions. These data sets are summarized in order of increasing system size and centrality in Table I. The online cut column refers to the multiplicity hardware centrality definition for the Si beam data and the forward energy definition for the Au beam data. Sets 1 and 2 are for π^+ pairs from a 14.6 A·GeV/c Si beam incident on a 1.63 g/cm² Al target (6% beam interaction length). Set 1 combines both peripheral TMA triggered data and minimum bias data. Set 2 includes only the minimum bias data. Sets 3–6 are for pion pairs from a Si beam incident on a 0.944 g/cm² Au target (1%). Two different TMA level-1 thresholds were used to collect negative pion pairs for peripheral and semi-peripheral events (sets 3 and 4). The central TMA trigger was used to collect pion pairs of both signs (sets 5 and 6). Negative pion pairs from 11.6 A·GeV/c Au+Au collisions were taken using the same Au target (1.5% interaction length for Au beam) for central triggers in 1992 (set 9), and for minimum bias events in 1994 (sets 7 and 8). The Au+Au minimum bias data set was divided at $E_{\text{ZCAL}} = 550$ in order to match the online centrality condition for data set 9. All data sets were subject to offline cuts to reject beam pile-up and to improve centrality definition. Table I gives the final pion pair statistics after all offline cuts.

The final TMA multiplicity and ZCAL forward energy

TABLE I: Summary of correlation data sets.

Set	System	Online Centrality	Offline Centrality	Pairs
1.	Si+Al $\rightarrow 2\pi^+ + X$	periph./m.b.	$N_{\text{TMA}} < 45$	83602
2.	Si+Al $\rightarrow 2\pi^+ + X$	min. bias	$N_{\text{TMA}} > 30$	78713
3.	Si+Au $\rightarrow 2\pi^- + X$	periph.	$N_{\text{TMA}} < 75$	50713
4.	Si+Au $\rightarrow 2\pi^- + X$	semi-periph.	$N_{\text{TMA}} < 115$	98468
5.	Si+Au $\rightarrow 2\pi^- + X$	central	$N_{\text{TMA}} > 75$	232296
6.	Si+Au $\rightarrow 2\pi^+ + X$	central	$N_{\text{TMA}} > 75$	76661
7.	Au+Au $\rightarrow 2\pi^- + X$	min. bias	$E_{\text{ZCAL}} > 550$	77837
8.	Au+Au $\rightarrow 2\pi^- + X$	min. bias	$E_{\text{ZCAL}} < 550$	88198
9.	Au+Au $\rightarrow 2\pi^- + X$	central	none	85573

distributions for all nine data sets are shown in Fig. 1. Only the ZCAL distributions are shown for the Au+Au system (sets 7–9) — a new multiplicity array (NMA) was in place for the collection of data in sets 7 and 8 but was not used in this analysis. The negative values in some of the E_{ZCAL} distributions were the results of excessive noise in the ZCAL electronics readout. This effect is taken into account in the centrality determination described in the next section.

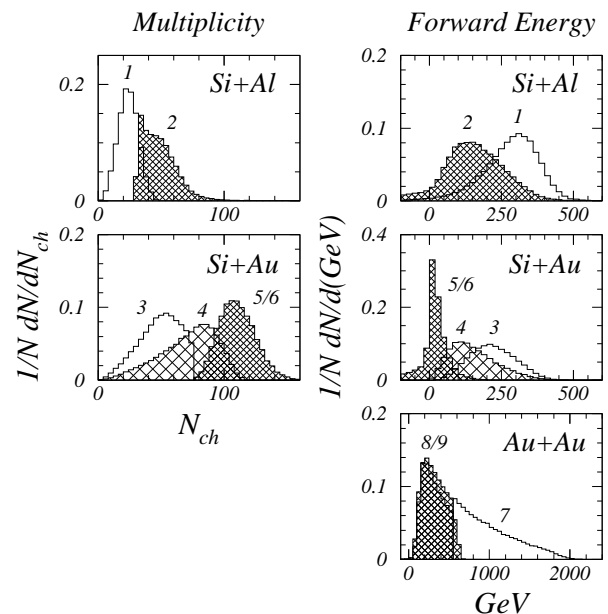


FIG. 1: TMA multiplicity and ZCAL forward energy distributions for all pion pair events. Central distributions are densely hatched, peripheral distributions are unfilled, and the Si+Au semi-peripheral distribution is sparsely hatched. Data set numbers from Table I are printed alongside the distributions. All distributions are normalized to unit area.

III. DATA REDUCTION

A. Centrality Determination

The forward energy distributions from ZCAL were used to determine the collision geometry for each system. The number of participant nucleons from the projectile is nominally calculated from the ZCAL forward energy (E_{ZCAL}) and the kinetic energy per nucleon ($E_{nucleon}$) according to,

$${}^{ZC}N_{proj} = A - \frac{E_{ZCAL}}{E_{nucleon}}. \quad (3.1)$$

In applying Eq. 3.1 to the data, negative E_{ZCAL} values were included in the average. The mean values for ${}^{ZC}N_{proj}^{1/3}$ are given in Table II.

To account for the effect of the excess noise in the ZCAL, and to obtain a more accurate determination of the collision geometry, a Monte Carlo Glauber model was used to simulate the forward energy distributions. We use a value of 30 mb for the N-N cross-section and the nuclear distributions are given by a Wood-Saxon distribution with nuclear radius, $r = 1.07A^{1/3}$ fm, and surface thickness 0.55 fm [23].

The ZCAL value for each Monte Carlo event in a given system was calculated by sampling from a Poisson distribution set by the beam distribution for the data. This distribution was then smeared with a Gaussian to simulate the additional noise observed in the distributions. The width of the Gaussian term (10–20 GeV) was chosen to match the noise in the target-out corrected minimum bias distribution while maintaining agreement for beam events.

The model was used to calculate distributions for the number of projectile, target, and total participants and the transverse rms distribution of binary collisions (ρ_{rms}). Each Monte Carlo event was assigned a weight according to its calculated ZCAL value, defined by the ZCAL distribution for 2π events divided by the minimum bias distribution. This weighting procedure is necessary to reproduce the correct ZCAL distribution for events with two pions in the spectrometer. The weighted distributions for the impact parameter and total participants are shown in Fig. 2. The mean values are listed in Table II. The average value of ${}^{ZC}N_{proj}$ calculated with Eq. 3.1 are similar to the values of N_{proj} calculated using the Glauber model. All geometric quantities are observed to increase with increasing centrality within each system. The geometric values are identical for the two central Si+Au data sets and nearly equivalent for the two central Au+Au data sets.

B. Pion identification and pair selection

The tracking algorithm for the 1991-1992 data (sets 1–6, 9) [24] began with a road-finder to connect TOF, TR1

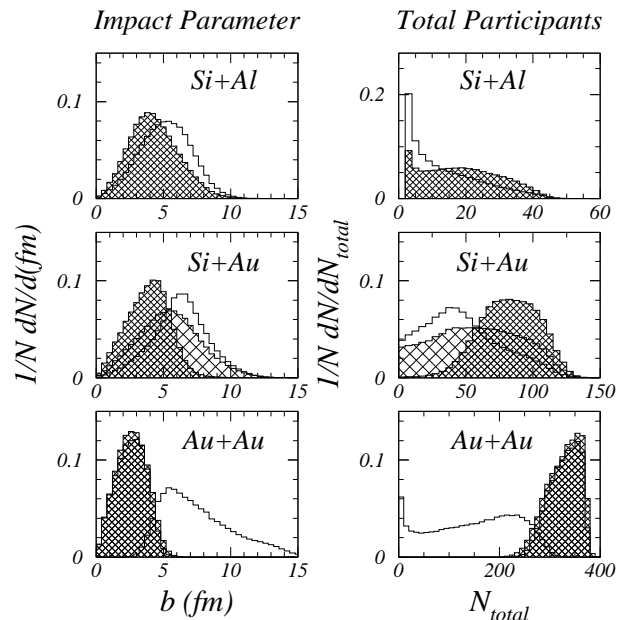


FIG. 2: Distributions for impact parameter (left) and total participants (right) from Monte Carlo Glauber model for all data sets. More central distributions are more densely hatched, as in Fig. 1.

TABLE II: Average geometric quantities calculated from ZCAL distributions and a Monte Carlo Glauber model. Participant numbers are raised to the one-third power and then averaged. The value for ρ_{rms} is the transverse rms distribution of all nucleon-nucleon interactions (in units of fm) averaged over all collisions.

System	Set	${}^{ZC}N_{proj}^{1/3}$	$N_{proj}^{1/3}$	$N_{targ}^{1/3}$	$N_{total}^{1/3}$	ρ_{rms}
Si+Al	1	1.94	1.76	1.75	2.20	1.15
	2	2.46	2.23	2.18	2.78	1.57
Si+Au	3	2.19	2.10	2.43	2.87	1.59
	4	2.49	2.43	2.94	3.42	1.85
	5	2.87	2.88	3.79	4.29	2.20
	6	2.87	2.88	3.79	4.29	2.21
Au+Au	7	4.40	3.95	3.97	5.00	2.52
	8	5.52	5.43	5.44	6.84	3.35
	9	5.45	5.48	5.46	6.89	3.36

and TR2 hits. Additional hits collected on the downstream tracking chambers were used to construct the downstream track segment. This was projected through the magnet using an effective dipole field approximation assuming a target vertex and hits were collected on T1 and T2. All hits associated with the track were fit with the vertex constraint removed. Tracks were required to pass goodness of fit cuts and to project to within 2 cm of the nominal target position. The single particle momentum resolution was determined by GEANT simulation and parameterized as $\sigma_p = ap/\beta \oplus bp^2$, with $a = 1.2\%$ and $b = 0.6\%$ (GeV/c) $^{-1}$. For the 1994 data (sets 7–

8) upstream track segments were found and fit independently using the additional hits on TRF1 and TRF2. The two track segments were then fit using the same magnetic field approximation, and applying the same vertex and goodness of fit cuts. Using additional information from TRF1 and TRF2 the momentum resolution for 1994 was improved to give $a = 0.85\%$ and $b = 0.12\%$ $(\text{GeV}/c)^{-1}$ [25].

Pions were identified up to a momentum of 1.85 GeV/c by requiring a unique association with a TOF hit, and a measured $1/\beta$ that lies within 3σ of the expected value for pions and outside of the 3σ band for kaons. The dominant background comes from electron contamination, determined to be less than 5% [26] in the region $0.54 < p < 1.3$ GeV/c. Pion pair momentum distributions for the central Si+Au and Au+Au data sets are shown in Fig. 3. The Si-beam data were taken with a spectrometer setting of 14 degrees, which covers an angular region from 14 to 28 degrees and leads to a mean pair-rapidity for pions approximately equal to $Y_{\text{NN}}=1.72$. For the Au-beam the spectrometer was rotated to 21 degrees, primarily to achieve lower track densities in the upstream chambers. The mean pion pair-rapidity for the Au-beam data is 1.43, slightly backwards of $Y_{\text{NN}} = 1.61$.

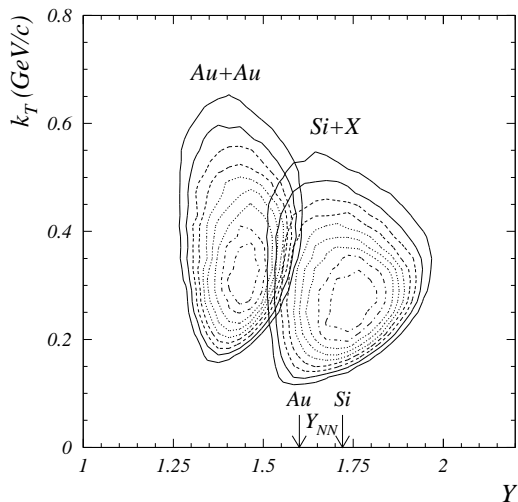


FIG. 3: Distributions in k_T and rapidity for Si+X (14° spectrometer setting) and Au+Au (21° setting). Arrows indicate rapidity for nucleon-nucleon center of mass for 14.6 A-GeV/c Si and 11.6 A-GeV/c Au beams.

The two-track resolution was determined separately for the 1991–1992 and 1994 tracking algorithms, by examining the ratio of signal to event-mixed pairs versus the relative slopes $\delta\theta_x$ and $\delta\theta_y$ upstream of the magnet. For the 1991–1992 data set, the two-track efficiency is well

parameterized by a two-dimensional Gaussian,

$$\varepsilon(\delta\theta_x, \delta\theta_y) = 1 - 0.86 \exp \left[-\frac{(2.75)^2 \delta\theta_x^2 + \delta\theta_y^2}{2(0.0121)^2} \right],$$

$$\delta\theta_x = p_{1x}/p_{1z} - p_{2x}/p_{2z},$$

$$\delta\theta_y = p_{1y}/p_{1z} - p_{2y}/p_{2z}. \quad (3.2)$$

A detailed GEANT simulation of two-pion events produced the same Gaussian widths for the two-track efficiency, but the coefficient for the exponential was closer to unity. One expects this coefficient to be less than unity in the data due to the presence of mis-associated hits from other tracks. The inverse of Eq. 3.2 was applied as a correction in the region where the efficiency was greater than $\sim 50\%$, defined as,

$$\sqrt{(2.75)^2 \delta\theta_x^2 + \delta\theta_y^2} > 0.011. \quad (3.3)$$

Pairs not in this region were removed from the analysis.

For the 1994 data (sets 7 and 8), the two-track efficiency is flat but then drops sharply for close tracks. For these data, no correction was applied and the two-track cut is given by,

$$\sqrt{\delta\theta_x^2 + \delta\theta_y^2} > 0.008. \quad (3.4)$$

IV. CORRELATION ANALYSIS

A. Parameterizations

Ideally the Bose-Einstein correlation function is defined to be the ratio of the probability for emitting two pions in the presence of Bose-Einstein symmetrization to the probability for the case with no symmetrization. The latter can be approximated using Monte Carlo or event mixing [27] techniques. For each data set, an event-mixed background was formed from pion pairs from different events chosen at random from the entire data set. The number of background pairs was chosen to be 5–10 times the signal to achieve statistical errors smaller than those for the signal, but still Poisson distributed [26]. This background differs from the ideal in two respects, it contains a residual correlation distortion first noted by Zajc [3], and it lacks two-body final state interactions such as the Coulomb interaction. The effect of the residual correlation is included in the systematic error estimates. We correct for the Coulomb interaction using an analytic approximation for the Coulomb wave function of two-pions emanating from a finite static source. This source is assumed to be a spherically symmetric Gaussian in the pair center-of-mass frame. This approximation has been described before [28] and is reviewed in Appendix B. The two-track cuts (Eq. 3.3 and 3.4) are applied to both the signal and background. Other final state interactions such as the di-pion strong interaction [29, 30] and the

Coulomb interaction with the nuclear remnant are expected to be negligible [31] and are not considered. The correlation function is then given by,

$$C_2(\mathbf{q}, k_T) = \frac{A(\mathbf{q}, k_T)}{B(\mathbf{q}, k_T)} \cdot \frac{1}{\varepsilon(\delta\theta_x, \delta\theta_y)} \cdot \frac{1}{F(\eta, Q_{\text{inv}}, R_{\text{inv}})}. \quad (4.1)$$

Here, A and B are the signal and event-mixed background, ε is the two-track efficiency defined by Eq. 3.2, and F is the Coulomb correction defined by Eq. B1. Q_{inv} is the magnitude of two-pion relative 4-momentum in the pair rest frame, and R_{inv} is the parameter returned by the 1-D invariant Gaussian parameterization,

$$C_2(Q_{\text{inv}}) = 1 + \lambda e^{-(Q_{\text{inv}}^2 R_{\text{inv}}^2)}. \quad (4.2)$$

Fits to this parameterization are used to perform an iterative determination of the Coulomb correction. Beginning with the assumption of a point source (i.e. Gamow correction), the R_{inv} parameter converges to within 1% after two iterations for all data sets.

The Yano-Koonin parameterization [32] is used to extract the longitudinal velocity of the source,

$$C_2(Q_{\text{inv}}, q_l) = 1 + \lambda e^{-(R^2 + \tau^2) \gamma_s^2 (q_0 - \beta_s q_l)^2 + (Q_{\text{inv}}^2 R^2)}, \quad (4.3)$$

where $q_l = p_{z1} - p_{z2}$ and β_s is the longitudinal component of the source velocity. R and τ are the spherically symmetric Gaussian radius and emission duration, respectively.

Using the source frames determined from the Yano-Koonin fits, all data sets were fit to the 3-D Bertsch-Pratt parameterization [10, 14],

$$C_2(q_l, q_s, q_o) = 1 + \lambda e^{(-q_l^2 R_l^2 - q_s^2 R_s^2 - q_o^2 R_o^2)}, \quad (4.4)$$

where q_l is the longitudinal component of the relative momentum from Eq. 4.3. The transverse relative momentum is separated into components perpendicular (q_s) and parallel (q_o) to the pion pair velocity. This parameterization measures the longitudinal and transverse correlation lengths, R_l and R_s , respectively. For an azimuthally symmetric source without dynamical correlations, the pion emission duration is calculated from R_o , R_s , and the transverse velocity of the pion pair, β_T ,

$$\tau = \sqrt{R_o^2 - R_s^2} / \langle \beta_T \rangle. \quad (4.5)$$

A variation of this parameterization suggested by Chapman [33], includes a cross-term, R_{lo} , which is expected to be non-vanishing for sources that are asymmetric in z ,

$$C_2(q_l, q_s, q_o) = 1 + \lambda e^{(-q_l^2 R_l^2 - q_s^2 R_s^2 - q_o^2 R_o^2 - 2q_l q_o R_{lo})}. \quad (4.6)$$

It is instructive to relate the cross-term to the Generalized Yano-Koonin parameterization (GYK) [12], using the relation, $q_o = \vec{q} \cdot \vec{\beta}_{pr}$.

$$\begin{aligned} C_2(q_l, q_T, q_o) &= 1 + \lambda e^{(-q_l^2 R_l^2 - q_T^2 R_T^2 - q_o^2 \tau^2)} \\ &= 1 + \lambda e^{(-q_l^2 (R_l^2 + \beta_l^2 \tau^2) - q_T^2 (R_T^2 + \beta_T^2 \tau^2) - 2q_l q_o \beta_l \beta_T \tau^2)}. \end{aligned} \quad (4.7)$$

This provides a simple explanation for the cross-term, R_{lo} in the absence of dynamical correlations, and illustrates why the cross-term vanishes for sources which are symmetric about the $z = 0$ plane.

B. Minimization

A new log-likelihood minimization function is used in this analysis. It assumes Poisson probability distributions for both signal and background, with means given by μ and ν respectively. The correlation function is defined as the ratio of these means by imposing a delta-function constraint on the conditional probability for C , given A and B ,

$$\begin{aligned} P(C|A, B) &= \int d\mu d\nu \left(\frac{\mu^A e^{-\mu}}{A!} \right) \left(\frac{\nu^B e^{-\nu}}{B!} \right) \delta(C - \mu/\nu) \\ &= \frac{C^A}{A!B!} \frac{(A+B+1)!}{(C+1)^{A+B+2}}. \end{aligned} \quad (4.8)$$

Taking the negative of twice the log and collecting leading order terms in A and B leads to the minimization function used in this analysis,

$$\chi^2_P = -2 \left[A \ln \left(\frac{C(A+B)}{A(C+1)} \right) + B \ln \left(\frac{A+B}{B(C+1)} \right) \right]. \quad (4.9)$$

Note that Eq. 4.9 approaches a chi-squared distribution, $\frac{(A-CB)^2}{\sigma_A^2 + \sigma_{CB}^2}$, in the limit of large A and B . We compare Eq. 4.9 to another log-likelihood minimization function commonly used [34],

$$\begin{aligned} \chi_{PML}^2 &= -2(C_2 B - A) - \\ &2(\sigma_A^2 + \sigma_{C_2 B}^2) \ln \left(\frac{(C_2 B - A) + (\sigma_A^2 + \sigma_{C_2 B}^2)}{(\sigma_A^2 + \sigma_{C_2 B}^2)} \right). \end{aligned} \quad (4.10)$$

This form also assumes a Poisson distributed signal for A , but the error terms for the background have been derived by working backwards from the chi-squared limit. All terms in Eq. 4.9 follow naturally from the assumption of Poisson distributions for A and B and the log-likelihood method. For this reason, the new minimization function may be more accurate for fits involving bins with small counts. However, both Eqs. 4.9 and 4.11 were shown to give consistent results in fits to the data. The minimization was performed using the MINUIT package [35].

V. RESULTS

For each of the nine data sets in Table I the three parameterizations, Q_{inv} , Yano-Koonin, and Bertsch-Pratt were performed in order. The Q_{inv} fits were used to determine the Coulomb correction. The longitudinal velocity of the source frames were obtained from the Yano-Koonin fits, and the HBT radii from the Bertsch-Pratt

fits were used in analysis of centrality, system, and k_T dependence. A complete set of tables for all fitted radii are given in Appendix C.

A. Q_{inv} Fit Results

Fit results for the final iteration Q_{inv} fits are summarized in Table VIII. Tables VIII through XV are found in Appendix C. These radii were taken as input to the Coulomb correction calculation for all subsequent multi-dimensional parameterizations for these data sets. For each system, R_{inv} increases with collision centrality. Table VIII also lists the mean transverse mass, $\langle m_T \rangle$, for each of the nine data sets. In calculating this mean, it is common to restrict the average to only those pairs with low relative momentum, which carry the information on the source dimensions. However, for systems that vary in size, the region of low relative momentum will also vary inversely with the source size. To account for this effect, the average restricted to the region $Q_{\text{inv}} < 2/R_{\text{inv}}$ using the step function Θ ,

$$\langle m_T^* \rangle = \frac{\sum_{i=1}^N \sqrt{(k_T^2)_i + m_\pi^2} \Theta(2/R_{\text{inv}} - (Q_{\text{inv}})_i)}{\sum_{i=1}^N \Theta(2/R_{\text{inv}} - (Q_{\text{inv}})_i)} \quad (5.1)$$

The quantity $\langle m_T^* \rangle$ should be sufficiently general to be used over a wide variation of system sizes and experimental acceptances. Table VIII shows that $\langle m_T^* \rangle$ is never less than 84% of $\langle m_T \rangle$ for these data. The fully corrected Q_{inv} correlation functions fits are shown in the left set of panels of Fig. 4.

B. Yano-Koonin Fit Results

By construction, the R and τ parameters of Eq. 4.3 are in the longitudinal rest frame of the source, and are invariant under longitudinal boosts. However, large longitudinal boosts yield q -distributions that are extended along a narrow ridge of the $q_l = q_0$ axis, and this presents a challenge for binning and minimization. This effect was studied with a Monte Carlo simulation and it was determined that there is a slight systematic bias in the fitted τ and β_s when the reference frame differs from the true source frame by more than a half unit of rapidity. The results of this study are given in Appendix A.

To minimize this bias, all data sets were initially fit in the Y_{NN} frame, 1.72 for the Si-beam and 1.60 for Au. Data sets with values of β_s which differed significantly from zero were then refit in the frames expected to yield $\beta_s = 0$. Only the Si+Au central data (sets 5 and 6) and Au+Au data (sets 7–9) required a second fit. The weighted means for β_s for the Si+Au central and Au+Au systems were -0.24 ± 0.03 and -0.15 ± 0.05 respectively. This led to the choice of the $Y = 1.50$ frame for central Si+Au, and the $Y = 1.45$ frame for Au+Au. Final fit frames and all parameters for the Yano-Koonin

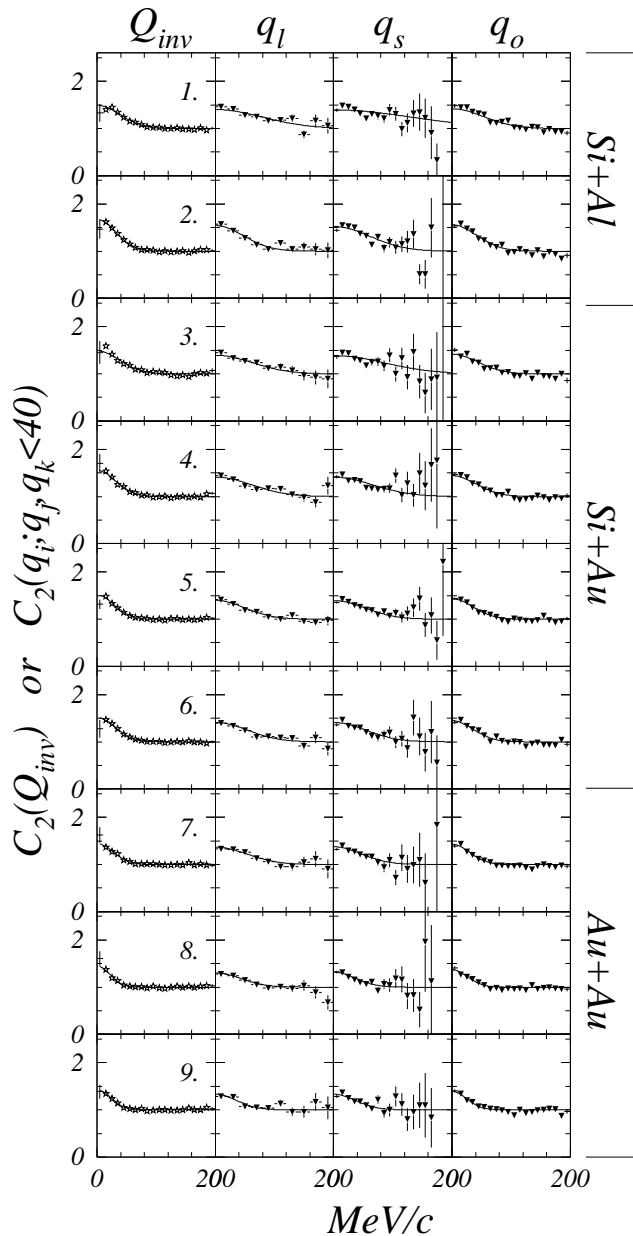


FIG. 4: Correlation functions for data sets 1–9. Data and parameterized fits for Q_{inv} (\star) are shown in left panels. Right panels show slices of the correlation functions and fits for Bertsch-Pratt parameterization (\blacktriangledown) for $q < 40$ MeV/c in the orthogonal variables.

fits are listed in Table IX. These frames are used for all remaining fits.

All final values for β_s are within two standard deviations of zero. As with the Q_{inv} results, the Yano-Koonin radius increases monotonically with centrality for all systems and from smaller systems to larger. The emission duration shows a similar but weaker dependence on system size and centrality. We note that because the acceptance for the Si-beam pairs centered at Y_{NN} (see Fig. 3),

the final values for β_s for the Si+Al and non-central Si+Au systems are consistent with both the assumptions of a fixed source at Y_{NN} and longitudinal boost invariance. The final values of β_s for the symmetric Au+Au system are closer to the mean pair rapidity of $Y = 1.43$ than to Y_{NN} and therefore imply a source that is longitudinally boost invariant. However, the values of β_s for the asymmetric Si+Au central system are indicative of a pion source shifted backwards to $Y = 1.50$ and are inconsistent with the assumption of longitudinal boost-invariance.

C. Bertsch-Pratt Fit Results

The results of the Bertsch-Pratt fits with and without the Chapman R_{l_0} cross-term are listed in Tables X and XI, respectively. The system and centrality dependence of the radii will be presented graphically in Sec. VD. The R_{l_0} cross-terms are consistent with zero for the symmetric systems measured at mid-rapidity, as expected. The largest values are for the Si+Au and Au+Au central systems, and only for the central Si+Au $\rightarrow 2\pi^-$ does the R_{l_0} term differ from zero by more than 2σ .

Slices of the correlation functions for the Bertsch-Pratt fits (no cross-term) for all systems in Table X are shown in the right three panels of Fig. 4. The slices in each q-component are averaged over $q_i < 40$ MeV/c in the orthogonal q-variables.

From the values of R_o and R_s in the Bertsch-Pratt fits we have extracted values for the emission duration, τ , using Eq. 4.5. These are compared to the corresponding emission duration parameters measured in the Yano-Koonin fits. Fig. 5 shows the two parameterizations give similar results, but with Yano-Koonin τ is smaller for the lighter systems. This trend is consistent with the assumption of spherical symmetry in Yano-Koonin, and the trend towards greater asymmetry ($R_l > R_s$) in the lighter systems. The Generalized Yano-Koonin (GYK) suggested in [12], which separates the transverse and longitudinal components of the source, is a logical extension to Eq. 4.3. Use of this parameterization in the future may lead to an improved correspondence between emission durations determined by the two methods. For the remaining sections τ is extracted from Eq. 4.5 and its error incorporates the R_o - R_s covariant term from the error matrix.

As a systematic check on the reference frames, Bertsch-Pratt fits were also performed in the Longitudinal Co-Moving System (LCMS) frame, defined as the local frame in which the longitudinal pair momentum is zero. These results are given in Table XII. All radii are consistent with the fixed frame fits to within two standard deviations. Large differences are not expected given that the fixed frames used in the previous fits were consistent with the pair LCMS for all but the Si+Au central system, and the rms width of pair rapidity distribution is small

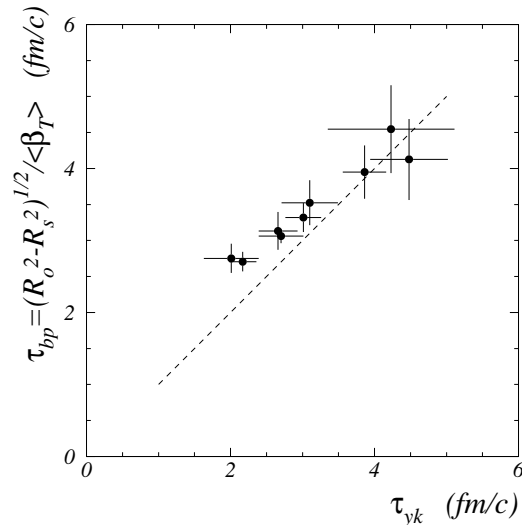


FIG. 5: Comparison between τ determined from Yano-Koonin and Bertsch-Pratt parameterizations. The dashed line indicates $\tau_{bp} = \tau_{yk}$.

TABLE III: Linear fits of Bertsch-Pratt radii to N_{proj} and N_{total} determined from Glauber model calculations.

Fit		R_l	R_s	R_o	τ
N_{proj}	a	1.44 ± 0.21	0.63 ± 0.31	1.48 ± 0.19	2.01 ± 0.23
	b	0.40 ± 0.07	0.63 ± 0.10	0.79 ± 0.07	0.45 ± 0.10
	χ^2/dof	18.2/7	8.4/7	10.5/7	5.6/7
N_{total}	a	1.27 ± 0.22	0.31 ± 0.34	1.43 ± 0.19	2.05 ± 0.22
	b	0.34 ± 0.05	0.54 ± 0.08	0.59 ± 0.05	0.32 ± 0.07
	χ^2/dof	12.6/7	2.8/7	6.3/7	6.3/7

(~ 0.1).

D. Centrality and System Dependence

We examine the dependence of the HBT radii on system size and centrality by comparing the Bertsch-Pratt radii given in Table X to the geometric quantities of Table II. Fig. 6 shows each of the radius parameters and the extracted emission duration plotted vs. mean values of $N_{proj}^{1/3}$ and $N_{total}^{1/3}$. The geometric dependences were fit to a linear form, $a + bx$. The extracted slopes and intercepts are given in Table III. R_s is also fit to a linear dependence on ρ_{rms} , yielding $a = -0.01 \pm 0.38$, $b = 1.19 \pm 0.18$, with a χ^2/dof of 3.5/7. All fitted parameters exhibit a linear dependence on both $N_{proj}^{1/3}$ and $N_{total}^{1/3}$. Converting R_s values to 3D rms radii ($\sqrt{3} \times R_s$) yields slopes of 0.99 ± 0.14 . and 1.20 ± 0.17 for $N_{total}^{1/3}$ and $N_{proj}^{1/3}$, respectively. The latter slope is consistent with the $A_p^{1/3}$ scaling noted by J. Bartke [18], where A_p denotes

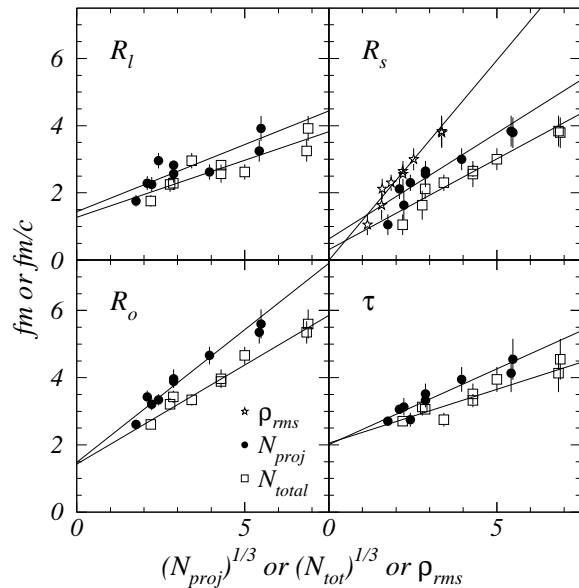


FIG. 6: Bertsch-Pratt radii and emission duration vs. projectile participants ($N_{\text{proj}}^{1/3}$), total participants ($N_{\text{total}}^{1/3}$), and the transverse rms distribution of binary collisions (ρ_{rms}). All radii are fit to a linear dependence of the form $a + bx$, with fit values given in Table III.

the atomic number of the projectile. This scaling dependence was taken from an analysis of mean-free paths of nuclear projectiles in emulsion [36, 37]. It is equivalent to the A-dependence of a hard sphere nuclear radius, and is consistent with measurements of the nuclear charge distribution in electron scattering [23]. The $N_{\text{total}}^{1/3}$ slopes for R_l are 60% smaller than for R_s , whereas for R_o they are 10% larger. In addition, the τ parameter also displays a significant slope that is consistent with the dependence of R_l .

We note that the rms values in reference [18] were derived from a variety of trigger conditions, parameterizations and regions of m_T , whereas in this analysis the parameterizations are uniform, the trigger conditions are accounted for, and the value of $\langle m_T^* \rangle$ is in the range of 300–325 MeV for Si+Al/Au and 350–360 MeV for Au+Au. The implication of the higher $\langle m_T^* \rangle$ range for Au+Au will be discussed in the next section.

The $N_{\text{total}}^{1/3}$ fits have a slightly lower χ^2/dof than the $N_{\text{proj}}^{1/3}$ fits. The success of the $N_{\text{total}}^{1/3}$, $N_{\text{proj}}^{1/3}$ and ρ_{rms} fits illustrates that there is more than one way to map the system/centrality onto geometry, and that the scaling of HBT radii need not be restricted to an effective radius of an assembly of wounded nucleons.

To translate the slopes and intercepts into a true geometric dependence of the pion source sizes requires a careful study of the m_T dependence of each radius. However, if the m_T dependence is largely independent of sys-

tem/centrality, one can extrapolate the entire scaling to lower m_T . Then the scaling observed at moderate values of m_T will also be valid at lower m_T value, where (for R_s) the geometric source is better approximated.

The intercepts for all R_s fits are consistent with zero, as one would expect for the dependence of a transverse overlap region that is extrapolated to zero participants. The intercepts for all other radius parameters differ significantly from zero. This is physically meaningful in the context of the standard interpretations given to these parameters, where R_l is indicative of the hadronization time, and R_o and τ are sensitive to the emission duration. Thus, even when extrapolating to zero participants, one may expect to measure finite lengths and durations for the pion hadronization.

E. Transverse Momentum Dependence

To study the transverse momentum dependence the central Si+Au $\rightarrow 2\pi^-$ data set was subdivided into three equal-statistics bins in m_T (sets a,c,e), and the Si+Au $\rightarrow 2\pi^+$ data set was subdivided into two equal bins (sets b,d). The two central Au+Au $\rightarrow 2\pi^-$ data sets were merged, and then divided into three equal bins (sets f,g,h). For this merged data set, the two-track cut of Eq. 3.4 was increased from 8 mrad to 15 mrad, and no two-track correction was applied. Fits to the full merged data set were performed for all parameterizations above and were found to be consistent with fits to the separate data sets. The data sets are given in Table XIII, along with the fit parameters and values for $\langle m_T^* \rangle$. The fully corrected Q_{inv} and Bertsch-Pratt correlation functions and fits are shown in Fig. 7.

The transverse momentum dependence of the two-pion correlation function has been discussed by many authors, [9, 13, 38, 39, 40, 41, 42], and in principle can be used to test dynamic models for rapidly expanding sources. We have found that the small number of k_T bins are insufficient to constrain these models. Instead we use an exponential form, $e^{(\alpha+\beta m_T)}$ to provide an empirical description of the m_T dependence of the Si+Au system, and use this to check the Au+Au system for consistency. Values for α and β are given in Table IV. Fig. 8 shows the m_T dependence for sets a–h, and for the Si+Au radii rescaled from $N_{\text{total}}^{1/3} = 2.87$ to $N_{\text{total}}^{1/3} = 6.89$ to match Au+Au. The solid line shows the m_T exponential fit also rescaled in this way. The Au+Au data points are consistent with the rescaled dependence for each radius.

Also shown are the E866 forward spectrometer results for π^- pairs from $1.9 < Y < 2.3$ for a centrality range that corresponds to the top 24% of the interaction cross-section gated on multiplicity [43, 44]. These data are less central than the Au+Au data set at mid-rapidity, which correspond to the top $\sim 15\%$ of the interaction cross-section gated on forward energy. For comparison, the forward spectrometer results are also shown rescaled up from $N_{\text{total}}^{1/3} = 6.3$, as determined from the Glauber model

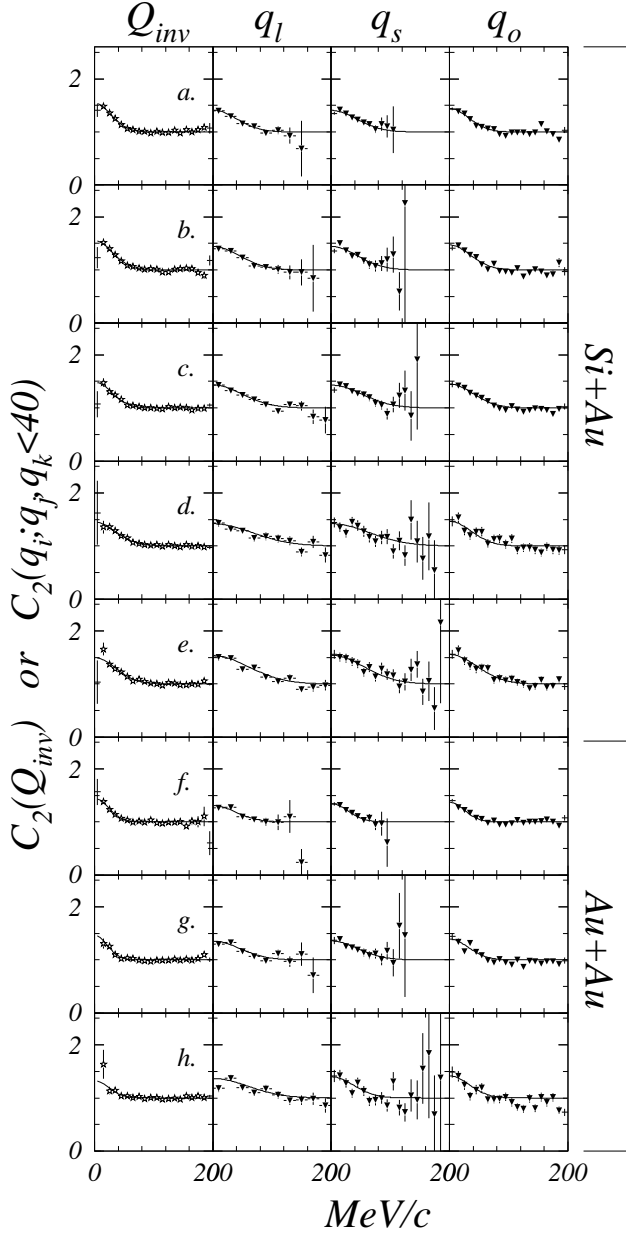


FIG. 7: Correlation functions for m_T data sets a–h. Data and parameterized fits for Q_{inv} (\star) are shown in left panels. Right panels show slices of the correlation functions and fits for Bertsch-Pratt parameterization (\blacktriangledown) for $q < 40$ MeV/c in the orthogonal variables.

calculations for the 24% most central collisions. Unlike the determination of $N_{total}^{1/3}$ for the other data sets, this was not done using the forward energy distributions for events containing 2-pions. This effect is largest for less central distributions, and therefore the rescaling of the forward rapidity radii in Fig. 8 should be taken as an upper bound. Overall, there is good agreement between the the rescaled Si+Au parameterized m_T dependence and the m_T dependence of the Au+Au radii at both for-

TABLE IV: Exponential fit parameters for m_T dependence in central Si+Au.

Variable	α	β	χ^2/dof
R_l	1.78 ± 0.21	-2.24 ± 0.61	1.7/3
R_s	1.53 ± 0.27	-1.47 ± 0.80	1.1/3
R_o	1.85 ± 0.16	-1.64 ± 0.49	2.3/3
τ	1.59 ± 0.64	-1.76 ± 2.05	4.9/3

ward and mid-rapidity.

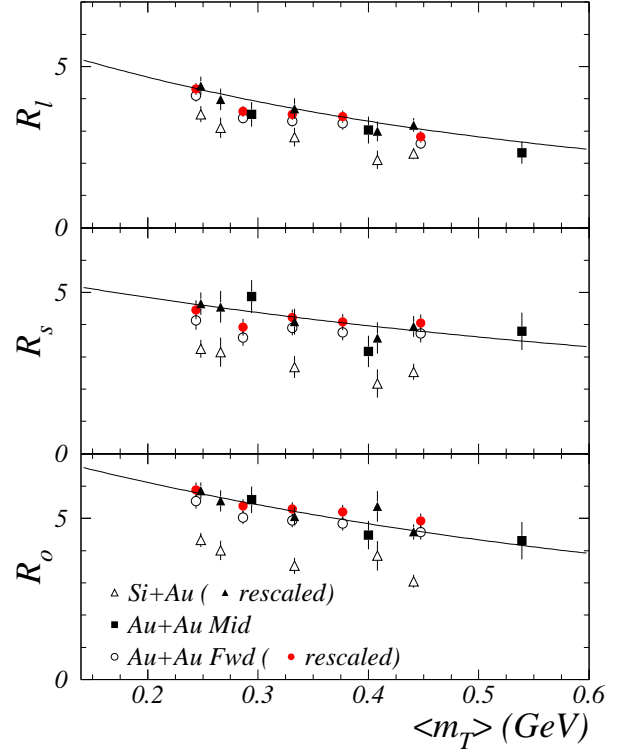


FIG. 8: m_T dependence of Bertsch-Pratt radii for Si+Au, Au+Au, Au+Au at forward rapidity [44], and for Si+Au rescaled by $N_{total}^{1/3}$ to match Au+Au. The solid line is a fit of the form $e^{(a+bm_T)}$ to the Si+Au points, rescaled according to the $N_{total}^{1/3}$ for Au+Au. The Au+Au forward rapidity data are also shown after being rescaled to match the mid-rapidity centrality condition.

The parameterized $\langle m_T^* \rangle$ dependence of Si+Au radii can now be used to check for errors arising from the 20% higher $\langle m_T^* \rangle$ values of the pion pairs for Au+Au used in the centrality analysis. The $\langle m_T^* \rangle$ dependence is used to interpolate all Bertsch-Pratt radii in Table X to a common value of $\langle m_T^* \rangle = 0.325$ GeV and the linear dependence on $N_{total}^{1/3}$ and $N_{proj}^{1/3}$ is refit. The results are given in Table V. The slopes for all parameters except τ increase slightly. All difference are less than the reported

TABLE V: Linear fits of Bertsch-Pratt radii to system/centrality dependence interpolated to $\langle m_T^* \rangle = 0.325$ GeV.

Fit		R_l	R_s	R_o	τ
N_{proj}	a	1.23 ± 0.21	0.45 ± 0.31	1.29 ± 0.20	1.91 ± 0.23
	b	0.47 ± 0.07	0.69 ± 0.10	0.86 ± 0.07	0.49 ± 0.10
	χ^2/dof	11.9/7	7.0/7	8.4/7	7.7/7
N_{total}	a	1.11 ± 0.22	0.16 ± 0.34	1.31 ± 0.20	2.01 ± 0.23
	b	0.38 ± 0.06	0.57 ± 0.08	0.62 ± 0.05	0.33 ± 0.07
	χ^2/dof	9.1/7	2.1/7	11.9/7	10.5/7

uncertainties, and the observations of the preceding section with respect to slopes and intercepts remain valid.

F. Centrality and Momentum

To investigate the centrality dependence for low and high regions of m_T , each of the data sets 1–7, and 8+9 combined ‘was divided into two m_T bins of equal statistics. The $\langle m_T^* \rangle$, R_{inv} , and Bertsch-Pratt radii for these fits are listed in Tables XIV and XV. The system and centrality dependence of the high and low m_T regions are shown in Fig. 9, plotted only for the N_{total} scaling. Independent linear fits to the two m_T regions are unable to resolve significant differences in the slopes and intercepts for the two regions. The data are compared to the $N_{\text{total}}^{1/3}$ linear fits (solid lines) for the full data sets that were shown in Fig. 6. The dashed lines are equal to the solid line fits interpolated up to 415 MeV and down to 275 MeV using the parameterized m_T dependence of Si+Au.

The high (low) m_T values for R_l and R_s fall below (above) the linear fits to full m_T regions, and are approximately consistent with the interpolations to higher (lower) m_T . For R_o the high m_T points are closer to the solid line, and the low m_T points fall slightly lower. For the τ parameter, nearly all points fall below the unbinned scaling. One possible explanation is a time-ordered pion emission, in which the high m_T pions are emitted at a time that is displaced relative to the emission of the low m_T pions. However, the potentially complex interplay between space, time, and momentum must be considered fully. At the very least, these results suggest a direction for future theoretical work and analysis with higher statistics measurements.

The ratio R_o/R_s has been suggested as way to search for changes in the pion emission duration [15] in heavy ion collisions. This ratio is plotted in Fig. 10 for the unbinned Si+Au central $2\pi^+$ (set 5) and Au+Au central data (set 8+9), and for these data sets subdivided into three m_T bins. The values of R_o/R_s vary from 1.2 to 1.5, but do not indicate any clear dependence on the m_T bin size. It may be interesting to repeat this study in the future with larger data samples and statistically

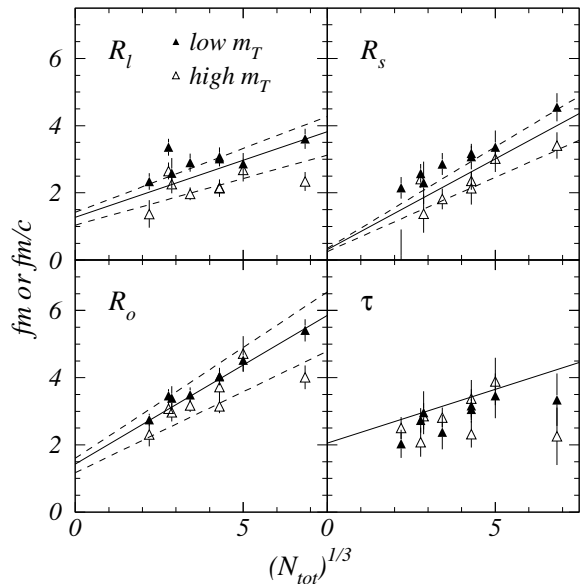


FIG. 9: Bertsch-Pratt radii and emission extracted duration vs. total participants ($N_{\text{total}}^{1/3}$) for high m_T (Δ) and low m_T (\blacktriangle) bins. The solid lines are linear fits to the full m_T range, and the dashed lines are the same linear fits rescaled to $\langle m_T^* \rangle$ of 275 MeV/c and 415 MeV/c.

independent bins of different sizes.

G. Systematic Errors

The systematic error in determining the centrality is expected to be dominated by the ZCAL noise. In the course of modifying the noise components in our model, we found nominal variations in the derived mean quantities to be consistent with a systematic error of approximately 5%.

The sources of systematic errors for the HBT radii are summarized in Table VI, and nominal values are given. The error due to finite momentum resolution was examined for the R_{inv} fit of the Au+Au central data set [45], and the effect of residual correlations in the background is reported elsewhere for the R_{inv} fit to the central Si+Au data set [46, 47]. The variation for the resolution smearing applies equally to each of the Bertsch-Pratt radii. All other variations are from R_{inv} parameterizations of the central Si+Au $\rightarrow 2\pi^-$ data set. The sign of the variation indicates the direction of the effect of incorporating the correction/change. Although some of the systematic errors enter with different signs, the different contributions are added in quadrature to yield a total systematic error of 3% for the radii and 5% for λ .

The effect of a partial Coulomb correction is considered separately in Appendix B. If a significant fraction of pairs

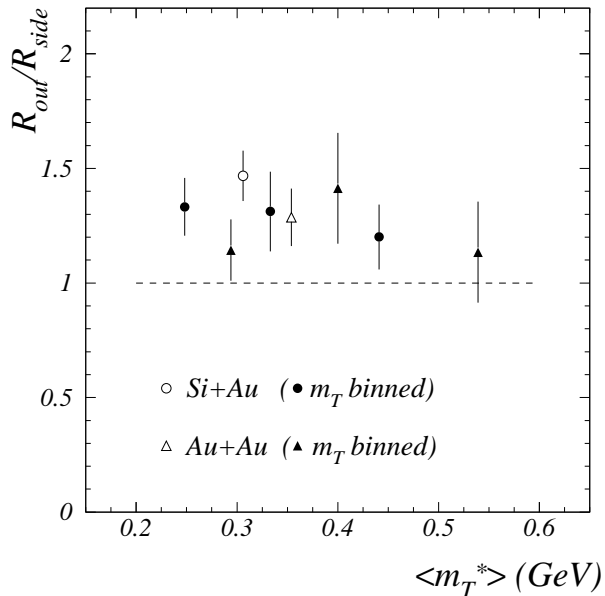


FIG. 10: The ratio of R_o/R_s for the high statistics data sets: central Si+Au (set 5, circles) and Au+Au (sets 8+9, triangles). The open symbols are for the full m_T range. The filled symbols are for the subdivision into three bins for Si+Au (sets a, c, e) and Au+Au (sets g, f, h).

TABLE VI: Sources and nominal values of systematic errors for the HBT radii and λ .

Source	R	λ
momentum resolution	+2%	+4%
5 MeV bins	$\pm 1\%$	$\pm 2\%$
residual correlation	-2%	+2%
two-track correction	$\pm 1\%$	$\pm 2\%$
Coulomb iteration	+0%	-1%
Coulomb resolution	-1%	-1%

(> 50%) are not subject to the Coulomb interaction, then this error would dominate for both R and λ .

VI. CONCLUSION

These data demonstrate unambiguously the strong connection that exists between the space-time measurements from Bose-Einstein correlations and collision geometry. All radii and lifetimes were observed to depend significantly on several measurements of system size and centrality. At $\langle m_T^* \rangle = 0.325$ GeV, R_s was observed to scale with the effective rms radius for the total number participants, as well as the linear transverse size in a Glauber model. For the R_l and τ parameters the linear dependence on $N_{\text{total}}^{1/3}$ is 60% weaker, and for R_o it is 10% stronger. Only R_s extrapolates to an intercept of zero.

The other parameters have finite intercepts of 1–2 fm for $N_{\text{proj}}^{1/3}, N_{\text{total}}^{1/3} = 0$.

Yano-Koonin fits were used to determine the longitudinal source velocities (β_s) for all systems. For all symmetric and non-central Si+Au systems measured at Y_{NN} , β_s is consistent with both a fixed source at Y_{NN} and a source which exhibits longitudinal boost invariance. The β_s for the Au+Au systems are only consistent with boost invariance, and for Si+Au central systems they imply a source that is shifted backwards of Y_{NN} .

The m_T dependence of the radii has been parameterized for central Si+Au and shown to be consistent with the central Au+Au m_T dependence at both mid and forward rapidity. For the first time, the system/centrality dependence was investigated independently for both high and low m_T regions.

The dependence of R_l and R_s with N_{total} at high and low m_T is consistent with interpolations based on the parameterized m_T dependence of the Si+Au central data. However, the R_o and τ radii are inconsistent with this interpolated m_T dependence, implying that these two parameters are sensitive to the width of the m_T bin. Finally, the ratio R_o/R_s is shown to be above unity for both the Si+Au and Au+Au central systems, and binning the data in m_T does not change this result.

Acknowledgments

The work was supported by the U.S. Department of Energy under contracts with ANL (W-31-109-ENG-38), BNL (DE-AC02-98CH10886), Columbia University (DE-FG0286-ER40281), LLNL (W-7405-ENG-48), MIT (DE-AC02-76ER03069), UC Riverside (DE-FG03-86ER40271), by NASA (NGR-05003-513), under contract with the University of California, by the Ministry of Education and KOSEF (951-0202-032-2), in Korea, and by the Ministry of Education, Science, Sports, and Culture of Japan.

We wish to thank E.P. Hartouni and S. Pratt for their support and for enlightening discussions. This paper is dedicated to the memory of Chuck Parsons, whose insight, ingenuity, and enormously creative spirit inspired a generation of graduate students on E859.

APPENDIX A: FRAME DEPENDENCE OF THE YANO-KOONIN PARAMETERIZATION

To study systematic effects of the Yano-Koonin parameterization a Monte Carlo sample of pion events was generated for a 3 fm spherically symmetric Gaussian source with lifetime 2 fm/c at $Y = 1.75$ in the lab. These simulated pairs were then fit to Eq. 4.3 while varying the fit frame (in which the q-variables were calculated) from $Y = 0.5$ to $Y = 3.0$ in steps of 0.25 units of rapidity. In all fits, the bin sizes were fixed at 20 MeV for q_l and 15 MeV for Q_{inv} and q_0 . Fig. 11 shows the results of this study

for the fitted radius, lifetime, and source frame. There

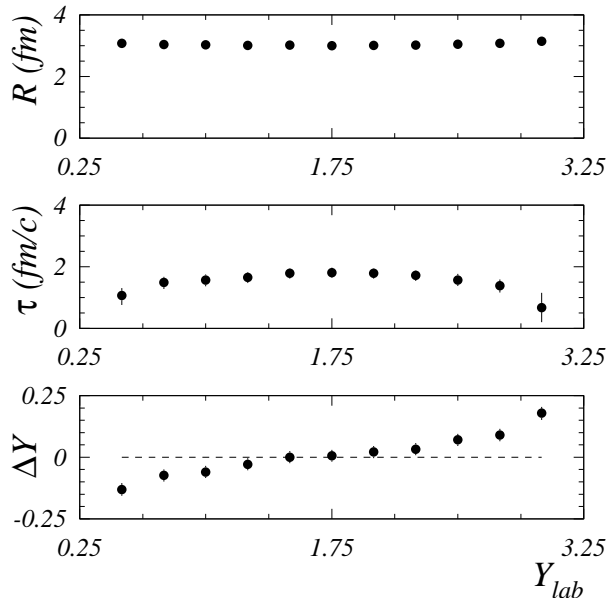


FIG. 11: Systematic dependence of Yano-Koonin fit parameters on reference frame for Monte Carlo Gaussian sources, with $R = 3$ fm, $\tau = 2$ fm/c and a source velocity corresponding to $Y = 1.75$. ΔY refers to the difference between the fit rapidity and the rapidity of the Monte Carlo Gaussian source.

is a systematic shift in the source frame that is approximately 10% of the difference between the fit frame and the actual source frame. In the simulation this difference is noticeable for differences as small as 0.25 units in rapidity. The change in source frame is correlated with a reduction in the measured lifetime, although R is observed to be stable for the region tested.

APPENDIX B: COULOMB CORRECTION

The Coulomb correction function used in this work is an analytic approximation to the full Coulomb wave calculation. The form of this correction is given by,

$$G(\eta) \times \left[1 + \eta P5(s) \frac{(1 + F(s))}{1 + e^{-s^2}} \right] \quad (\text{B1})$$

where G is the standard Gamow correction for a point source, and $P5$ is a fifth order polynomial in the dimensionless quantity s ,

$$G(\eta) = \frac{2\pi\eta}{e^{2\pi\eta} - 1} \quad (\text{B2})$$

$$\eta = 2\mu\alpha/Q_{\text{inv}} \quad (\text{B3})$$

$$s = R_{\text{inv}}Q_{\text{inv}}/\hbar \quad (\text{B4})$$

$$P5(s) = \frac{2}{\sqrt{\pi}} \min(\pi, 8(s - 5s^3/9 + 52s^5/225)) \quad (\text{B5})$$

where, μ is the reduced mass of the pion pair and α is the fine structure constant. The full form of the integral equation that was solved is described elsewhere [28], and the FORTRAN code for the tabulated function $F(s)$ is available upon request [48].

The accuracy of this analytic approximation (Eq. B1) is demonstrated in Fig. 12 by comparing the correction function for a 5 fm source to the Coulomb Wave integration calculated by the Correlation After Burner code (CRAB) [49]. Fig. 12 shows a significant difference between the full Coulomb correction and the Gamow correction, but the fast approximation shows good agreement with the calculation from CRAB.

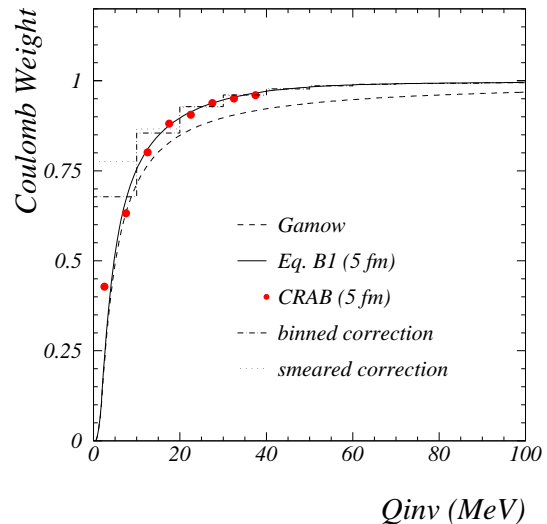


FIG. 12: Coulomb corrections for a point source (Gamow), a 5 fm spherically symmetric Gaussian calculated with (CRAB) and Eq. B1. The dashed histogram shows the effect of averaging Eq. B1 over the Si+Au data (set 5), and the dot-dashed histogram incorporates the effect of momentum resolution smearing.

The effect of resolution smearing was estimated by evaluating Eq. B1 for the event-mixed background, but applying the Coulomb weight at the value of Q_{inv} returned by a spectral response function. The form of the response function was parameterized in momentum and polar angle spread according to Monte Carlo single particle distributions [46]. Fig. 12 shows the Coulomb correction histogram — weighted background divided by background — with and without the response function. The effect of the response function is evident only in the lowest bin (0-10 MeV/c), and introduced a 1% reduction in the 3D HBT radii and λ values. Given the small size of the effect, it was incorporated into the overall systematic error estimate, but the correlation fits used the unsmearred correction.

If the deviation of λ from unity is caused by a substantial fraction of pions from long lived resonances, it is possible that the effect of the Coulomb interaction will

TABLE VII: Bertsch-Pratt fit parameters for full, half, and no Coulomb correction.

Parameter	full	half	none
λ	0.645 ± 0.045	0.397 ± 0.019	0.354 ± 0.020
R_l	2.96 ± 0.23	2.53 ± 0.15	2.32 ± 0.17
R_s	2.30 ± 0.24	2.21 ± 0.21	1.93 ± 0.23
R_o	3.34 ± 0.17	3.94 ± 0.13	3.79 ± 0.16
χ^2/dof	3266.3/3540	4270.6/4298	4284.8/4298

also be reduced in strength. To understand the magnitude of this effect, the Si+Au $\rightarrow 2\pi^-$ data sets were fit with a half-strength Coulomb correction, and also with no Coulomb correction. The results are summarized in Table VII. Variations in the radii are as large as 20% for R_l and R_o , and λ is greatly affected. A thorough investigation of effect of long lived resonances on the Coulomb correction is left for further study.

APPENDIX C: TABLES OF CORRELATION RADII

Tables VIII through XV show the complete set of fitted radii used to study the system, centrality, and transverse mass dependence for the Q_{inv} , Yano-Koonin, and Bertsch-Pratt fits of the 14.6 A·GeV/c Si+Al, Si+Au, and 11.6 A·GeV/c Au+Au data sets. All R and τ parameters are given in units of fm and fm/c, respectively.

TABLE VIII: Q_{inv} fit parameters and $\langle m_T \rangle$ for data sets 1–9.

System	Set	$\langle m_T \rangle$	$\langle m_T^* \rangle$	λ	R_{inv}	χ^2/dof
Si+Al	1	0.348	0.327	0.491 ± 0.029	3.59 ± 0.16	32.1/27
	2	0.349	0.319	0.676 ± 0.040	4.42 ± 0.16	20.8/27
Si+Au	3	0.345	0.323	0.487 ± 0.039	3.70 ± 0.23	46.6/27
	4	0.345	0.313	0.551 ± 0.035	4.47 ± 0.18	45.0/27
	5	0.342	0.306	0.511 ± 0.026	4.91 ± 0.15	39.2/27
	6	0.349	0.316	0.514 ± 0.041	4.54 ± 0.22	11.5/27
Au+Au	7	0.411	0.361	0.441 ± 0.039	5.13 ± 0.28	24.1/27
	8	0.410	0.348	0.451 ± 0.051	6.55 ± 0.43	31.3/27
	9	0.420	0.358	0.428 ± 0.046	6.09 ± 0.38	24.8/26

TABLE IX: Yano-Koonin fit parameters for data sets 1–9.

System	Set	Y_{fit}	λ	R	τ	β	χ^2/dof
Si+Al	1	1.72	0.452 ± 0.024	1.74 ± 0.13	2.17 ± 0.19	-0.06 ± 0.06	3770.7/4044
	2	1.72	0.627 ± 0.035	2.75 ± 0.14	2.01 ± 0.38	-0.08 ± 0.07	3901.9/3992
Si+Au	3	1.72	0.467 ± 0.024	2.17 ± 0.11	2.66 ± 0.27	-0.04 ± 0.05	3357.6/3605
	4	1.72	0.503 ± 0.028	2.45 ± 0.16	2.70 ± 0.31	-0.03 ± 0.06	4048.3/4156
	5	1.50	0.499 ± 0.022	2.83 ± 0.09	3.01 ± 0.25	-0.06 ± 0.05	4588.6/4844
	6	1.50	0.515 ± 0.038	2.76 ± 0.20	3.10 ± 0.39	0.07 ± 0.07	3811.3/4055
Au+Au	7	1.45	0.496 ± 0.031	2.84 ± 0.14	3.86 ± 0.30	0.01 ± 0.07	4234.2/4407
	8	1.45	0.454 ± 0.044	3.36 ± 0.27	4.48 ± 0.54	-0.12 ± 0.08	4382.3/4503
	9	1.45	0.530 ± 0.053	3.96 ± 0.25	4.23 ± 0.88	0.11 ± 0.10	4136.8/4486

TABLE X: Bertsch-Pratt fit parameters for data sets 1–9. Values for τ are calculated from Eq. 4.5 with R_s – R_o covariances used in error propagation.

System	Set	λ	R_l	R_s	R_o	τ	χ^2/dof
Si+Al	1	0.437 ± 0.024	1.76 ± 0.17	1.05 ± 0.31	2.61 ± 0.13	2.71 ± 0.14	3507.3/3594
	2	0.645 ± 0.045	2.96 ± 0.23	2.30 ± 0.24	3.34 ± 0.17	3.13 ± 0.26	3266.3/3540
Si+Au	3	0.452 ± 0.034	2.25 ± 0.22	1.63 ± 0.43	3.21 ± 0.18	3.06 ± 0.10	3053.2/3184
	4	0.488 ± 0.036	2.29 ± 0.21	2.12 ± 0.30	3.43 ± 0.18	2.75 ± 0.20	3382.1/3636
	5	0.503 ± 0.021	2.82 ± 0.14	2.65 ± 0.18	3.89 ± 0.13	3.32 ± 0.20	4274.9/4298
	6	0.517 ± 0.054	2.57 ± 0.27	2.56 ± 0.39	3.97 ± 0.28	3.52 ± 0.31	3544.5/3672
Au+Au	7	0.506 ± 0.037	2.62 ± 0.23	3.00 ± 0.33	4.66 ± 0.26	3.95 ± 0.37	2942.1/3114
	8	0.480 ± 0.043	3.25 ± 0.32	3.84 ± 0.46	5.35 ± 0.33	4.13 ± 0.56	3070.2/3236
	9	0.536 ± 0.047	3.92 ± 0.37	3.79 ± 0.45	5.60 ± 0.43	4.55 ± 0.61	2694.4/3095

TABLE XI: Q_{inv} and Bertsch-Pratt fit parameters with R_{l_o} cross-term (see Eq. 4.6) for data sets 1–9.

System	Set	λ	R_l	R_s	R_o	R_{l_o}	χ^2/dof
Si+Al	1	0.430 ± 0.023	1.65 ± 0.17	0.97 ± 0.31	2.59 ± 0.13	0.58 ± 0.36	3441.8/3604
	2	0.618 ± 0.034	2.71 ± 0.19	2.20 ± 0.23	3.29 ± 0.15	0.51 ± 0.69	3363.7/3533
Si+Au	3	0.426 ± 0.034	2.03 ± 0.23	1.26 ± 0.49	3.15 ± 0.24	0.74 ± 0.82	3260.6/3200
	4	0.479 ± 0.028	2.16 ± 0.18	2.01 ± 0.26	3.41 ± 0.16	0.68 ± 0.68	3303.2/3643
	5	0.496 ± 0.021	2.75 ± 0.14	2.59 ± 0.18	3.86 ± 0.13	2.59 ± 0.75	4126.7/4293
	6	0.496 ± 0.037	2.47 ± 0.24	2.47 ± 0.31	3.93 ± 0.24	0.50 ± 0.94	3498.9/3621
Au+Au	7	0.499 ± 0.036	2.55 ± 0.23	2.90 ± 0.32	4.66 ± 0.26	-1.34 ± 1.29	2919.7/3170
	8	0.464 ± 0.040	3.18 ± 0.37	3.50 ± 0.45	5.37 ± 0.22	4.58 ± 2.37	3018.2/3264
	9	0.582 ± 5.033	4.49 ± 1.15	3.71 ± 1.00	5.74 ± 1.09	-3.10 ± 3.08	3018.2/3264

TABLE XII: LCMS frame Bertsch-Pratt fit parameters for the for data sets 1–9.

System	Set	λ	R_l	R_s	R_o	χ^2/dof
Si+Al	1	0.359 ± 0.022	1.42 ± 0.22	0.00 ± 0.48	2.53 ± 0.14	3365.7/3503
	2	0.531 ± 0.041	2.68 ± 0.25	2.00 ± 0.27	3.35 ± 0.19	3163.2/3478
Si+Au	3	0.359 ± 0.038	1.96 ± 0.30	0.90 ± 0.82	3.12 ± 0.26	3113.5/3107
	4	0.392 ± 0.028	1.97 ± 0.22	1.57 ± 0.37	3.41 ± 0.17	3206.7/3551
	5	0.398 ± 0.023	2.66 ± 0.19	2.23 ± 0.23	4.05 ± 0.17	3835.7/4199
	6	0.413 ± 0.042	2.43 ± 0.31	2.11 ± 0.46	4.17 ± 0.27	3261.9/3447
Au+Au	7	0.399 ± 0.043	2.28 ± 0.30	2.54 ± 0.46	4.77 ± 0.38	3002.2/3084
	8	0.347 ± 0.037	2.75 ± 0.36	3.11 ± 0.57	5.49 ± 0.39	3034.3/3188
	9	0.392 ± 0.042	3.49 ± 0.44	3.05 ± 0.56	6.05 ± 0.58	2714.5/3033

TABLE XIII: Q_{inv} and Bertsch-Pratt fit parameters for m_T -dependent data sets a–h.

System	Set	R_{inv}	$\langle m_T^* \rangle$	λ	R_l	R_s	R_o	τ	χ^2/dof
Si+Au	a	5.03 ± 0.21	0.248	0.560 ± 0.035	3.52 ± 0.25	3.25 ± 0.28	4.33 ± 0.22	3.32 ± 0.35	1834.6/1844
	b	4.69 ± 0.29	0.266	0.577 ± 0.059	3.10 ± 0.31	3.15 ± 0.45	4.01 ± 0.30	2.75 ± 0.54	2036.9/2083
	c	4.84 ± 0.29	0.333	0.530 ± 0.064	2.81 ± 0.29	2.69 ± 0.34	3.53 ± 0.25	2.49 ± 0.40	2796.6/3007
	d	3.94 ± 0.34	0.408	0.512 ± 0.075	2.11 ± 0.28	2.18 ± 0.44	3.84 ± 0.46	3.32 ± 0.53	3705.3/3657
	e	3.93 ± 0.25	0.441	0.628 ± 0.058	2.30 ± 0.17	2.54 ± 0.25	3.05 ± 0.20	1.78 ± 0.49	4296.6/4230
Au+Au	f	6.05 ± 0.38	0.294	0.544 ± 0.055	3.62 ± 0.38	4.90 ± 0.51	5.57 ± 0.41	2.92 ± 0.93	1261.7/1215
	g	6.68 ± 0.85	0.400	0.479 ± 0.073	3.05 ± 0.42	3.11 ± 0.54	4.39 ± 0.44	3.32 ± 0.64	1960.6/2010
	h	5.76 ± 1.09	0.539	0.508 ± 0.101	2.36 ± 0.34	3.73 ± 0.57	4.21 ± 0.54	2.10 ± 1.44	3541.3/3693

TABLE XIV: Q_{inv} and Bertsch-Pratt fit parameters for low- m_T data sets 1–9.

System	Set	$\langle m_T^* \rangle$	R_{inv}	λ	R_l	R_s	R_o	χ^2/dof
Si+Al	1	0.277	3.38 ± 0.19	0.502 ± 0.038	2.34 ± 0.25	2.15 ± 0.32	2.75 ± 0.18	1867.9/1849
	2	0.271	4.37 ± 0.20	0.685 ± 0.044	3.36 ± 0.25	2.58 ± 0.28	3.46 ± 0.20	1789.6/1854
Si+Au	3	0.270	4.23 ± 0.31	0.500 ± 0.070	2.59 ± 0.45	2.30 ± 0.63	3.39 ± 0.36	1589.0/1699
	4	0.269	4.45 ± 0.21	0.569 ± 0.042	2.90 ± 0.27	2.86 ± 0.33	3.49 ± 0.22	1796.6/1859
	5	0.264	5.01 ± 0.17	0.539 ± 0.027	3.02 ± 0.18	3.18 ± 0.22	4.05 ± 0.17	2939.3/2981
	6	0.268	4.72 ± 0.29	0.576 ± 0.046	3.07 ± 0.28	3.08 ± 0.38	4.03 ± 0.26	2105.1/2151
Au+Au	7	0.309	5.20 ± 0.33	0.522 ± 0.051	2.87 ± 0.32	3.36 ± 0.50	4.52 ± 0.35	1305.1/1427
	8+9	0.308	6.08 ± 0.37	0.542 ± 0.041	3.61 ± 0.30	4.55 ± 0.42	5.41 ± 0.33	1640.1/1532

TABLE XV: Q_{inv} and Bertsch-Pratt fit parameters for high- m_T data sets 1–9.

System	Set	$\langle m_T^* \rangle$	R_{inv}	λ	R_l	R_s	R_o	χ^2/dof
Si+Al	1	0.410	3.58 ± 0.26	0.429 ± 0.039	1.37 ± 0.41	0.13 ± 0.78	2.31 ± 0.35	3491.7/3590
	2	0.411	4.28 ± 0.24	0.760 ± 0.069	2.65 ± 0.25	2.41 ± 0.26	3.08 ± 0.21	3428.1/3534
Si+Au	3	0.411	2.98 ± 0.23	0.472 ± 0.072	2.26 ± 0.27	1.38 ± 0.57	2.97 ± 0.27	3187.4/3165
	4	0.411	3.93 ± 0.31	0.519 ± 0.052	1.97 ± 0.19	1.82 ± 0.31	3.17 ± 0.19	3523.8/3633
	5	0.411	4.31 ± 0.24	0.573 ± 0.064	2.15 ± 0.20	2.36 ± 0.27	3.15 ± 0.21	4840.6/4986
	6	0.412	3.90 ± 0.34	0.495 ± 0.079	2.14 ± 0.26	2.14 ± 0.49	3.72 ± 0.42	3669.6/3654
Au+Au	7	0.485	4.24 ± 0.47	0.644 ± 0.089	2.68 ± 0.34	3.02 ± 0.40	4.72 ± 0.52	3174.5/3113
	8+9	0.485	6.44 ± 0.85	0.465 ± 0.056	2.34 ± 0.28	3.41 ± 0.39	4.01 ± 0.35	3581.9/3701

-
- [1] G. Goldhaber et al., Phys. Rev. **120**, 300 (1960).
[2] S. Fung et al., Phys. Rev. Lett. **41**, 1592 (1978).
[3] W. Zajc et al., Phys. Rev. C **29**, 2173 (1984).
[4] C. Adler et al., Phys. Rev. Lett. **87**, 082301 (2001).
[5] K. Adcox et al., to be published in Phys. Rev. Lett. (2002), nucl-ex/0201008.
[6] T. Csörgő, Heavy Ion Phys. **15**, 1 (2002), hep-ph/0001233.
[7] U. Wiedemann and U. Heinz, Phys. Rep. **319**, 145 (1999).
[8] R. H. Brown and R. Twiss, Phil. Mag. **45**, 663 (1954).
[9] S. Pratt, Phys. Rev. Lett. **53**, 1219 (1984).
[10] S. Pratt, Phys. Rev. D **33**, 1314 (1986).
[11] A. Makhlin and Y. Sinyukov, Z. Phys. C **39**, 69 (1988).
[12] S. Chapman, J. Nix, and U. Heinz, Phys. Rev. C **52**, 2694 (1995).
[13] U. Wiedeman, P. Scotto, and U. Heinz, Phys. Rev. C **53**, 918 (1996).
[14] G. Bertsch and G. Brown, Phys. Rev. C **40**, 1830 (1989).
[15] D. Rischke and M. Gyulassy, Nucl. Phys. **A608**, 479 (1996).
[16] M. Lisa et al., Phys. Rev. Lett. **84**, 2798 (2000).
[17] U. Wiedeman, Phys. Rev. C **57**, 266 (1998).
[18] J. Bartke, Phys. Lett. **B174**, 32 (1986).
[19] T. Abbott et al., Nucl. Instrum. Meth. A **290**, 41 (1990).
[20] K. Shigaki et al., Nucl. Instrum. Meth. A **282**, 41 (1999).
[21] D. Beavis et al., Nucl. Instrum. Meth. A **281**, 367 (1989).
[22] W. Zajc, in *Proceedings of the Fourth Conference on the Intersections between Particle and Nuclear Physics*, edited by W. V. Oers (AIP, Tucson Arizona, 1992).
[23] R. H. B. Hahn, D.G. Ravenhall, Phys. Rev. **101**, 1131 (1956).
[24] P. Rothschild, Ph.D. thesis, M.I.T. (1994).
[25] F. Wang, Ph.D. thesis, Columbia University (1996).
[26] R. Soltz, Ph.D. thesis, M.I.T. (1994).
[27] G. I. Kopylov, Phys. Lett. **B50**, 472 (1974).
[28] L. Ahle et al., Nucl. Phys. **A610**, 213c (1996).
[29] M. Suzuki, Phys. Rev. D **35**, 3359 (1987).
[30] Bowler, Z. Phys. C **39**, 81 (1988).
[31] P. Kopylov, Sov. Jour. Nucl. Phys. **15**, 219 (1972).
[32] F. Yano and S. Koonin, Phys. Lett. **B78**, 556 (1978).
[33] S. Chapman, P. Scotto, and U. Heinz, Phys. Rev. Lett. **74**, 4400 (1995).
[34] W. Zajc, in *Correlations and Multiparticle Production*, edited by R. W. M. Plumer, S. Raha (World Scientific Press, Singapore, 1991).
[35] CERN Program Library Long Write-up, D506 (1994).
[36] I. Tanihata, Tech. Rep. 85-10, GSI (1985).
[37] H. Heckman et al., Phys. Rev. C **17**, 1735 (1978).
[38] Y. Sinyukov, Nucl. Phys. **A498**, 151c (1989).
[39] S. Chapman et al., Heavy Ion Phys. **1**, 1 (1995), hep-ph/9409349.
[40] S. Chapman and R. Nix, Phys. Rev. C **54**, 866 (1996).
[41] M. Herrmann and G. Bertsch, Phys. Rev. C **51**, 328 (1995).
[42] U. Wiedeman and U. Heinz, Phys. Rev. C **56**, 3265 (1997).
[43] R. Soltz et al., Nucl. Phys. **661A**, 439c (1999).
[44] J. Lee, in *Proceedings of the 2nd Catania Relativistic Ion Study, Acicastello, Italy* (World Scientific, 1998), p. 309.
[45] L. Klatsky, B.S. thesis, M.I.T. (1997).
[46] V. Cianciolo, Ph.D. thesis, M.I.T. (1994).
[47] Y. Akiba et al., Phys. Rev. Lett. **70**, 1057 (1993).
[48] Request from mbaker@bnl.gov or soltz@llnl.gov.
[49] [Http://www.nscl.msu.edu/~pratt/freecodes/crab](http://www.nscl.msu.edu/~pratt/freecodes/crab).